CHAPTER IV

NUMERICAL SOLUTIONS

This chapter is concerned with the numerical results obtained from the solution scheme described in Chapter III. A computer program has been developed to investigate the interaction between a rigid circular cylinder and a homogeneous poroelastic half space. First, the convergence and stability of numerical solutions are investigated. The accuracy of the present solution is verified by comparing with the existing solution. Numerical results are presented to demonstrate the applicability of the present solution scheme and to portray the influence of governing parameters on the interaction problem. The discussion on these results is also given in this chapter.

4.1 Numerical Solution Scheme

The solution scheme described in Chapter III is implemented into a computer program. The tasks performed by the computer program can be summarized as:

1. A set of unknown forces are assumed to be applied at N node points on an auxiliary surface S . The boundary conditions at N node points on S are specified.
2. The influence functions are determined to establish the discrete version of equations (3.51) and (3.53) for a permeable contact surface, and, equations (3.51) and (3.54) for an impermeable one with respect to N and N node points on S and S , respectively. These equations are then solved for unknown forces at N node points on an auxiliary surface S by using equation (3.61).
3. The complete poroelastic field on the boundary S as well as at points in Ω can be computed directly from equations (3.51) to (3.54).

The major computation effort performed by the computer program is the evaluation of influence functions. The influence functions G_{ij} and H_{ij} appear in terms of semi-infinite integrals with a complex-valued integrand involving Bessel functions. These integrals can not be evaluated analytically. To carry out semi-infinite

integration numerically, it is important to examine the dominant characteristics of the integrand. The main singularities of the integrand are the branch points defined by γ_i $(i=1,2,3)$ given by equations (3.32) and (3.33), and the pole denoted by R given by equation (A.18). For a poroelastic half-space, the branch points are given by L_1, L_2 and S, i.e., the wave numbers corresponding to three kinds of body waves defined in equations (3.36), (3.37) and (3.38), respectively, while poles are given by the roots of (A.18) which is the Rayleigh equation for a poroelastic half-space governing the propagation of the surface waves. In reality, all poroelastic materials have some internal friction (i.e. $b \neq 0$). The presence of material damping results in branch points and poles of the integrands which are complex-valued quantities. Therefore, the real ξ-axis is free from any singularities and the influence functions can be evaluated by direct numerical integration along the real ξ-axis.

Another important feature concerning the integrand is the rate of decay which actually decides the upper limit, ξ_L, to be employed for the numerical integration. The exponential function in the integrand will play the most important role. There are two cases when slow decay occurs: (1) when both observation and source points are near the surface, i.e. $(z+z')$ approaches zero; and (2) when the difference between the depth of observation point and the depth of source is very small, i.e. $|z-z'|$ approaches zero. In these two cases the integration must be calculated up to a very large value of ξ_L in order to get sufficient convergence of the solution. The first situation can be avoided if the generating source is restricted to a depth greater than zero at all times. Suppose the minimum value of z' is z_0 then the convergence of the solution for the most critical point, i.e. observation point at surface, can be checked. Similarly, suppose the minimum value of $|z-z'|$ is d_0, if the difference between the depth of the observation point and the source is greater than d_0, the convergence of the particular solution can also be assured.

For the numerical evaluation of influence function, the globally adaptive numerical quadrature scheme is used. The scheme subdivides the interval of integral and uses a 21-point Gauss-Kronrod rule (Piessens et al., 1983) to estimate the integral over each subinterval. The error for each subinterval is estimated by comparison of

the result obtained by 21-point Gauss-Kronrod rule with that by 10-point Gauss quadrature rule. The subinterval with the largest estimated error is then bisected and this procedure is applied to both halves. This bisection procedure is continued until the error criterion is reached.

4.2 Convergence and Numerical Stability

The convergence and stability of the numerical solution scheme described in the previous section are investigated with respect to the following parameters:

1. The upper limit of integration, ξ_L, used in the numerical integration of the semi-infinite integrals of influence functions.
2. The distance between surface S and S' denoted by Δa (see figure 3.1)
3. The number of nodes N and N' used to discretize the generating suface S and S', respectively. (see figure 3.2)

Figures 4.1 to 4.3 present the convergence of non-dimensional influence functions of a homogeneous poroelastic half-space with respect to ξ_L. The vertical ring load, radial ring load and ring fluid source of radius $0.9a$ and intensity f_0 per unit length are applied at a depth a below the free surface of a half-space at a frequency $\delta = 1.0$. The properties of the half-space are : $\lambda^* = 1.0$, $M^* = 12.2$, $\rho^* = 0.53$, $m^* = 1.1$, $\alpha = 0.97$ and $b = 2.3$. The value of influence functions are computed at radius a and depth $1.5a$,$1.05a$ and $1.005a$, respectively. It is found that the influence functions are converged at $\xi_L \geq 30$, 400, 5000 for $|z - z'| = 0.5a, 0.05a$ and $0.005a$, respectively.

Table 4.1 to 4.4 present the convergence of numerical solutions for K_v by varying N, N' and Δa for various slenderness ratios ($h/a = 0.5$, 2, 10 and 20) at a frequency $\delta = 5$. The properties of the half-space are : $\lambda^* = 1.0$, $M^* = 12.2$, $\rho^* = 0.53$, $m^* = 1.1$, $\alpha = 0.97$ and $b = 30$. It is found that solutions converge for $N = 30$ and $N' = 60$ with $\Delta a = 0.1$ for a short cylinder ($h/a \leq 2$)and $N = 40$ and $N' = 80$ with $\Delta a = 0.1$-0.25 for a long cylinder ($h/a \geq 10$).

4.3 Comparison with Existing solutions

The accuracy of the present solution scheme is verified by comparing the solution obtained from the present scheme with the existing solutions. Figure 4.4 presents a comparison of vertical impedance of a rigid cylinder embedded in an elastic half-space with different length/radius ratio (h/a = 0.25, 0.5, 1, 2) between the solutions given by Apsel and Luco (1987) and the present solutions. The results are obtained by the degeneration of a poroelastic medium to an elastic medium (the values of M^*, ρ^*, m^*, b^* and α are set to 10^{-4}).In addition, the material attenuation of 1% is added to the elastic modulus to ensure that the numerical integration along the real ξ-axis is free from any singularity (Senjuntichai and Rajapakse, 1994). It can be observed that the present solutions are in excellent agreement with those given by Apsel and Luco and the maximum difference is about 3 percent. The accuracy of the present solutions is confirmed through this comparison.

In order to investigate the efficiency of the present scheme, a modified solution scheme based on a non-uniform body force field acting on the extended half-space is presented (Rajapakse and Shah, 1987). In this method, a poroelastic half-space containing an embedded cylinder in decomposed into an extended half-space and a fictitious bar as shown in figure 4.5. In order to account for the case of a short bar, it is assumed that V^* is subjected to body forces and concentrated load transfer represented by tractions acting on the terminal cross-section at $z = 0$ and h. To ensure that volume V^* deforms as a rigid body, it is assumed that the magnitude of body forces varies in both the r- and z-directions, and the tractions vary in the r-direction. The magnitude of body forces and tractions are determined by discretizing V^* and terminal cross-sections using hollow cylindrical and base elements as shown in figure 4.6.This results in the following flexibility and equilibrium equations

$$\sum_{j=1}^{M_1}\left[\bar{f}_{rr}(r_i,z_i;r_j,z_j)B_{rj}+\bar{f}_{rz}(r_i,z_i;r_j,z_j)B_{zj}\right]$$

$$+\sum_{j=1}^{M_2}\left[f_{rr}(r_i,z_i;r_j,z_j)T_{rj}+f_{rz}(r_i,z_i;r_j,z_j)T_{zj}\right]=0 \qquad (4.1)$$

$$\sum_{j=1}^{M_1}\left[\bar{f}_{zr}(r_i,z_i;r_j,z_j)B_{rj}+\bar{f}_{zz}(r_i,z_i;r_j,z_j)B_{zj}\right]$$

$$+\sum_{j=1}^{M_2}\left[f_{zr}(r_i,z_i;r_j,z_j)T_{rj}+f_{zz}(r_i,z_i;r_j,z_j)T_{zj}\right]-\Delta_z=0 \tag{4.2}$$

$$\sum_{j=1}^{M_1}B_{zj}2\pi r_j\Delta z_j\Delta r_j+\sum_{j=1}^{M_2}T_{zj}2\pi r_j\Delta r_j+(\rho-\rho_b)\pi a^2\omega^2 h\Delta_z=P_0 \tag{4.3}$$

In equations (4.1)-(4.3), M_1 is the number of hollow cylindrical elements, M_2 is the number of base element, $\bar{f}_{ij}$ and f_{ij} are displacements in i-direction due to unit body forces and unit traction acting in j-direction, respectively. B_{rj} and B_{zj} represent magnitude of body forces acting on the jth hollow cylindrical element, T_{zj} and T_{rj} are magnitude of tractions acting on the jth base element.

Figure 4.7 show comparison of vertical impedance of a rigid cylinder in an elastic half-space between present solutions from indirect boundary integral equation method and non-uniform body force method with existing solutions presented by Apsel and Luco (1987). It can be observed that the results from both schemes are in good agreement with the solutions given by Apsel and Luco (1987) and the maximum error is about 6% maximum for non-uniform body force method and only 3% for indirect boundary integral equation method as discussed earlier. In order to ensure that volume V^* deforms as a rigid body, the solutions based on the non-uniform body force method requires the discretization of volume V^* into several hollow cylindrical elements. Obviously, the non-uniform body force method demands much more computational time than the indirect boundary integral equation method.

4.4 Numerical Results and Discussion

The numerical solutions shown in sections 4.2 and 4.3 confirm the convergence, numerical stability and accuracy of the present formulation. In this section, various numerical results are presented to demonstrate the influence of various parameters on the dynamic response of the cylinder. The rigid cylinder considered in the numerical study is subjected to axisymmetric time-harmonic

loading as shown in Figure 1.1. A non-dimensional frequency δ in the range $0 < \delta \leq 6.0$ is considered in the numerical study. In addition, the non-dimensional parameters $\lambda^* = 1.0$, $M^* = 12.2$, $\rho^* = 0.53$, $m^* = 1.1$ and $\alpha = 0.97$ are used for all numerical results presented in this section.

Figures 4.8 and 4.9 show the non-dimensional vertical impedance of impermeable and fully permeable rigid cylinders with different length/radius ratio (h/a=0.5, 2, 10 and 20). In addition, two values of b^*, i.e., $b^* = 2.3$ and 30 are considered. It is found that the variation of the impedance with non-dimensional frequency δ is smooth for all h/a. In addition, for long cylinders ($h/a \geq 10$), the real part of the impedance shows steep increase with δ at very low frequency. It is also clearly seen from Figures 4.8 and 4.9 that the vertical impedance depends significantly on h/a. The impedance increases with increasing the ratio of *h/a*. This is due to the fact that the contact surface between the cylinder and the medium is increased for a longer cylinder. As a result, the longer cylinder will have more resisting force than the shorter one. Another feature of the solutions in Figure 4.8 and 4.9 are the increasing difference between impedance of impermeable and fully permeable cylinder at high frequencies (δ>1). However, the difference seems to be decreased when the cylinder becomes longer.

Figures 4.10 and 4.11 show the non-dimensional vertical impedance of impermeable and fully permeable rigid cylinder embedded in four different poroelastic materials. The properties of the poroelastic materials are $b^* = 0.001$, 2.3, 10 and 30. The poroelastic medium with a larger value of b^* shows slightly higher stiffness at the initial low frequency δ<0.5. The vertical impedance of impermeable and fully permeable cylinders are nearly identical for 0<δ<1.0 and become more different at higher frequency. In addition, The difference of Re(K_V) between impermeable and fully permeable cylinders decreases with increasing b^*. Since b^* is inversely proportional to permeability, it implies that material with b^* =0.001 is the most permeable and the material with b^* = 30 is the least permeable among the four poroelastic materials.

Figures 4.12 and 4.13 show the non-dimensional vertical impedance of impermeable rigid cylinder embedded in an elastic half-space ($\lambda^* = 1.0$) and four

different poroelastic materials defined previously. The variation of the imaginary parts with δ is nearly linear. Highest damping is found to occur in the material with highest value of b^* ($b^* = 30$). The difference in the impedances between a rigid cylinder in poroelastic materials and an elastic material becomes substantial at high frequency ($\delta > 1.0$) indicating the importance of poroelastic effect in dynamic soil-structural interaction analysis. The material parameter b quantifying the fluid viscous dissipation is found to have the most significant influence on the non-dimensional impedances when compared to other material parameters. Let consider the case where the poroelastic material properties are $\lambda = 1.0\ \ 10^8\ N/m^2$, $\mu = 1.0\ \ 10^8\ N/m^2$, $M = 12.2\ \ 10^8\ N/m^2$, $\rho = 2.0\ \ 10^3\ kg/m^3$, $\rho_f = 1.06\ \ 10^3\ kg/m^3$, $m = 2.2\ \ 10^3\ kg/m^3$, $b = 4.11\ \ 10^6\ N\,s/m^4$ and $\alpha = 0.97$. In addition, $V_0 = 1.0\ \ 10^6\ N$, $L = 8.0\ m$ and $a = 0.25\ m$. In this case, if the machine can operate when vertical displacement is less than 4 *mm*, the required non-dimensional vertical impedance (K_V) must be more than 10.0. From Figure 4.12, it is found that the frequency of excitations will be less than $\delta = 1.0$ or 142 *Hz*.

The present solution scheme can also be employed in the analysis of other axisymmetric foundations. Three types of foundations, i.e., hemisphere, taper and step as shown in figure 4.14 are considered. Figure 4.15 and 4.16 show the non-dimensional vertical impedance of the four different rigid foundations (i.e. cylinder, hemisphere, taper and step) in a poroelastic half-space by setting $h = 1$, $h_1 = 0.5$, $a = 1$ and $\bar{a} = 0.5$ in figure 4.14. The solutions are presented for both permeable and impermeable foundations. The properties of the poroelastic material are $\lambda^* = 1.0$, $M^* = 12.2$, $\rho^* = 0.53$, $m^* = 1.1$ and $\alpha = 0.97$ with $b^* = 2.3$ and 10. Comparison of impedances indicates that the real parts of all foundations for both fully permeable and impermeable surfaces slowly increase in the range $0 < \delta < 0.5$ and thereafter the impedances of impermeable foundations decrease gradually with increasing δ. The imaginary parts of impedances, on the other hand, increase with increasing frequency for $0 < \delta < 6$. It is also found that the imaginary parts for both permeable and impermeable foundations are almost identical when $0 < \delta < 2$. When $\delta > 2$, $\mathrm{Im}(K_V)$ for impermeable foundations are higher than those of permeable ones.

Table 4.1 Convergence of vertical impedance of rigid cylinder in a poroelastic medium with N, N' and Δa ($h/a = 0.5, \delta = 5, b^* = 30$)

(N, N')	K_v (permeable)							
	$\Delta a = 0.05$		$\Delta a = 0.1$		$\Delta a = 0.15$		$\Delta a = 0.2$	
	Re	Im	Re	Im	Re	Im	Re	Im
(20,10)	5.37	47.93	5.49	48.21	5.36	46.39	4.85	43.76
(40,20)	8.04	56.04	7.33	53.56	7.04	51.75	6.45	50.10
(60,30)	8.48	57.16	7.92	55.30	7.62	53.93	15.14	58.39
(80,40)	8.71	57.75	8.26	56.21	8.94	56.04	159.33	-130.69

(N, N')	K_v (impermeable)							
	$\Delta a = 0.05$		$\Delta a = 0.1$		$\Delta a = 0.15$		$\Delta a = 0.2$	
	Re	Im	Re	Im	Re	Im	Re	Im
(20,10)	-10.91	61.43	-11.72	63.12	-11.84	61.89	-11.80	61.67
(40,20)	-11.96	65.21	-11.90	64.75	-11.90	64.30	-11.90	64.06
(60,30)	-12.05	65.66	-11.97	65.34	-11.93	65.00	-12.20	65.62
(80,40)	-12.06	65.86	-11.99	65.57	-11.43	65.51	32.99	68.84

Table 4.2 Convergence of vertical impedance of rigid cylinder in a poroelastic medium with N, N' and Δa ($h/a = 2, \delta = 5, b^* = 30$)

(N, N')	K_v (permeable)							
	$\Delta a = 0.1$		$\Delta a = 0.15$		$\Delta a = 0.2$		$\Delta a = 0.25$	
	Re	Im	Re	Im	Re	Im	Re	Im
(20,10)	3.65	75.47	5.42	75.09	5.88	77.13	6.06	77.36
(40,20)	10.40	94.83	9.57	92.09	8.94	89.74	8.45	87.70
(60,30)	11.55	97.98	10.80	95.69	10.19	93.73	9.72	92.08
(80,40)	12.15	99.48	11.48	97.59	10.89	95.90	10.38	94.10

(N, N')	K_v (impermeable)							
	$\Delta a = 0.1$		$\Delta a = 0.15$		$\Delta a = 0.2$		$\Delta a = 0.25$	
	Re	Im	Re	Im	Re	Im	Re	Im
(20,10)	-3.02	104.56	-1.33	102.03	-1.05	101.20	-0.99	100.77
(40,20)	-3.42	107.20	-3.19	106.56	-3.04	106.04	-2.91	105.65
(60,30)	-3.76	108.47	-3.62	108.01	-3.52	107.64	-3.44	107.32
(80,40)	-3.89	109.03	-3.76	108.64	-3.70	108.34	-3.59	108.11

Table 4.3 Convergence of vertical impedance of rigid cylinder in a poroelastic medium with N, N' and Δa ($h/a = 10, \delta = 5, b^* = 30$)

(N, N')	K_v (permeable)							
	$\Delta a = 0.1$		$\Delta a = 0.15$		$\Delta a = 0.2$		$\Delta a = 0.25$	
	Re	Im	Re	Im	Re	Im	Re	Im
(20,10)	28.87	122.39	24.86	117.47	29.93	150.19	36.78	197.08
(40,20)	46.82	279.32	41.93	268.18	38.84	282.74	36.27	295.71
(60,30)	38.95	312.96	36.35	313.62	34.93	316.39	35.08	316.96
(80,40)	39.94	328.69	37.22	328.82	36.70	327.39	35.94	318.58
(100,50)	40.64	338.76	37.43	328.74	36.85	327.87	36.52	327.10

(N, N')	K_v (impermeable)							
	$\Delta a = 0.1$		$\Delta a = 0.15$		$\Delta a = 0.2$		$\Delta a = 0.25$	
	Re	Im	Re	Im	Re	Im	Re	Im
(20,10)	54.31	319.43	44.85	328.60	43.20	325.72	42.58	324.52
(40,20)	29.02	345.32	34.95	343.26	34.62	345.47	32.56	346.00
(60,30)	32.19	350.72	33.23	351.52	31.10	351.07	30.86	350.24
(80,40)	32.26	354.21	29.48	354.55	29.43	353.89	29.95	351.71
(100,50)	29.25	356.77	28.90	355.90	28.94	355.12	29.05	354.41

Table 4.4 Convergence of vertical impedance of rigid cylinder in a poroelastic medium with N, N' and Δa ($h/a = 20, \delta = 5, b^* = 30$)

(N, N')	K_v (permeable)							
	$\Delta a = 0.1$		$\Delta a = 0.15$		$\Delta a = 0.2$		$\Delta a = 0.25$	
	Re	Im	Re	Im	Re	Im	Re	Im
(20,10)	8.63	36.45	5.71	45.65	6.71	55.15	11.74	69.61
(40,20)	60.77	312.80	41.23	280.57	33.95	296.68	50.60	380.41
(60,30)	78.57	503.39	65.71	530.23	67.55	535.85	71.61	560.06
(80,40)	83.45	597.50	75.33	590.93	72.95	596.34	72.83	605.68
(100,50)	78.00	625.11	75.67	623.88	74.53	615.20	73.98	618.01

(N, N')	K_v (impermeable)							
	$\Delta a = 0.1$		$\Delta a = 0.15$		$\Delta a = 0.2$		$\Delta a = 0.25$	
	Re	Im	Re	Im	Re	Im	Re	Im
(20,10)	56.99	435.51	45.29	488.89	57.01	537.35	63.94	593.55
(40,20)	119.32	597.87	107.15	613.34	100.53	620.31	94.93	625.56
(60,30)	85.07	642.18	87.84	648.80	86.73	654.06	79.33	657.40
(80,40)	71.21	657.67	75.53	657.57	73.28	659.99	70.48	660.57
(100,50)	70.25	663.53	72.93	663.48	69.53	662.67	68.99	660.86

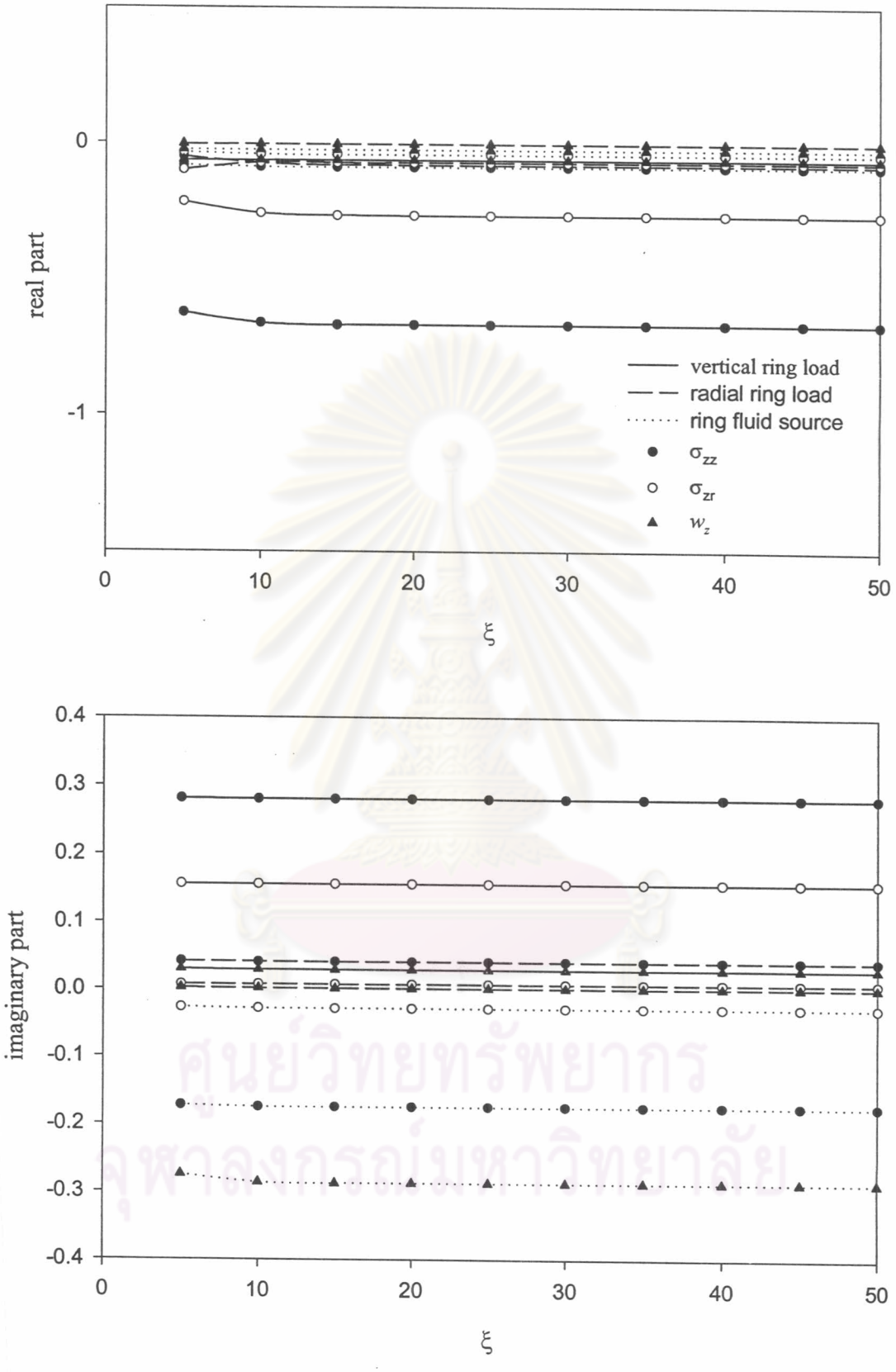

Figure 4.1 Convergence of influence functions subjected to vertical ring load, radial ring load and ring fluid source with respect to ξ_L $\left(|z-z'|=0.5\right)$

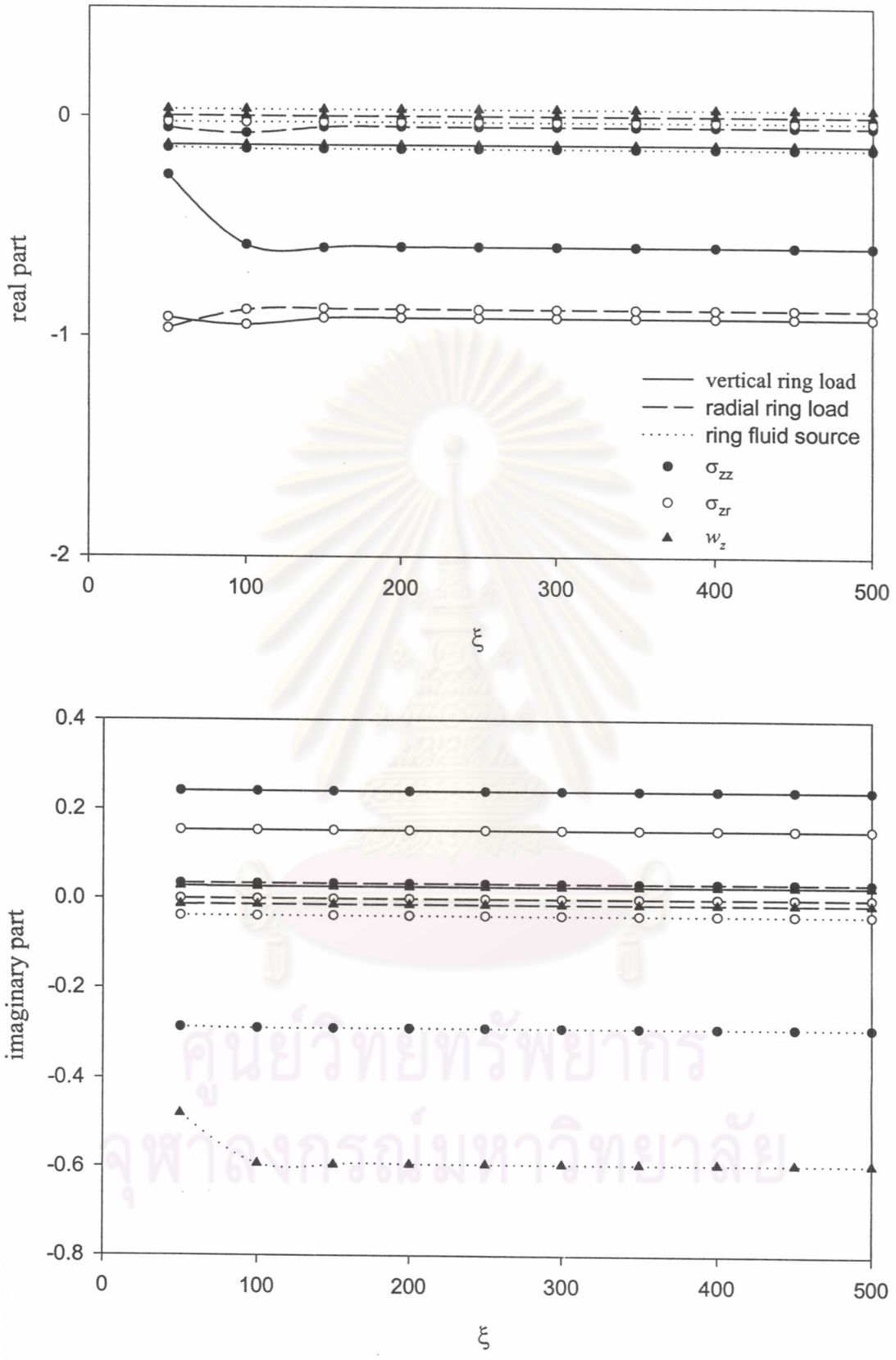

Figure 4.2 Convergence of influence functions subjected to vertical ring load, radial ring load and ring fluid source with respect to ξ_L $\left(|z-z'|=0.05\right)$

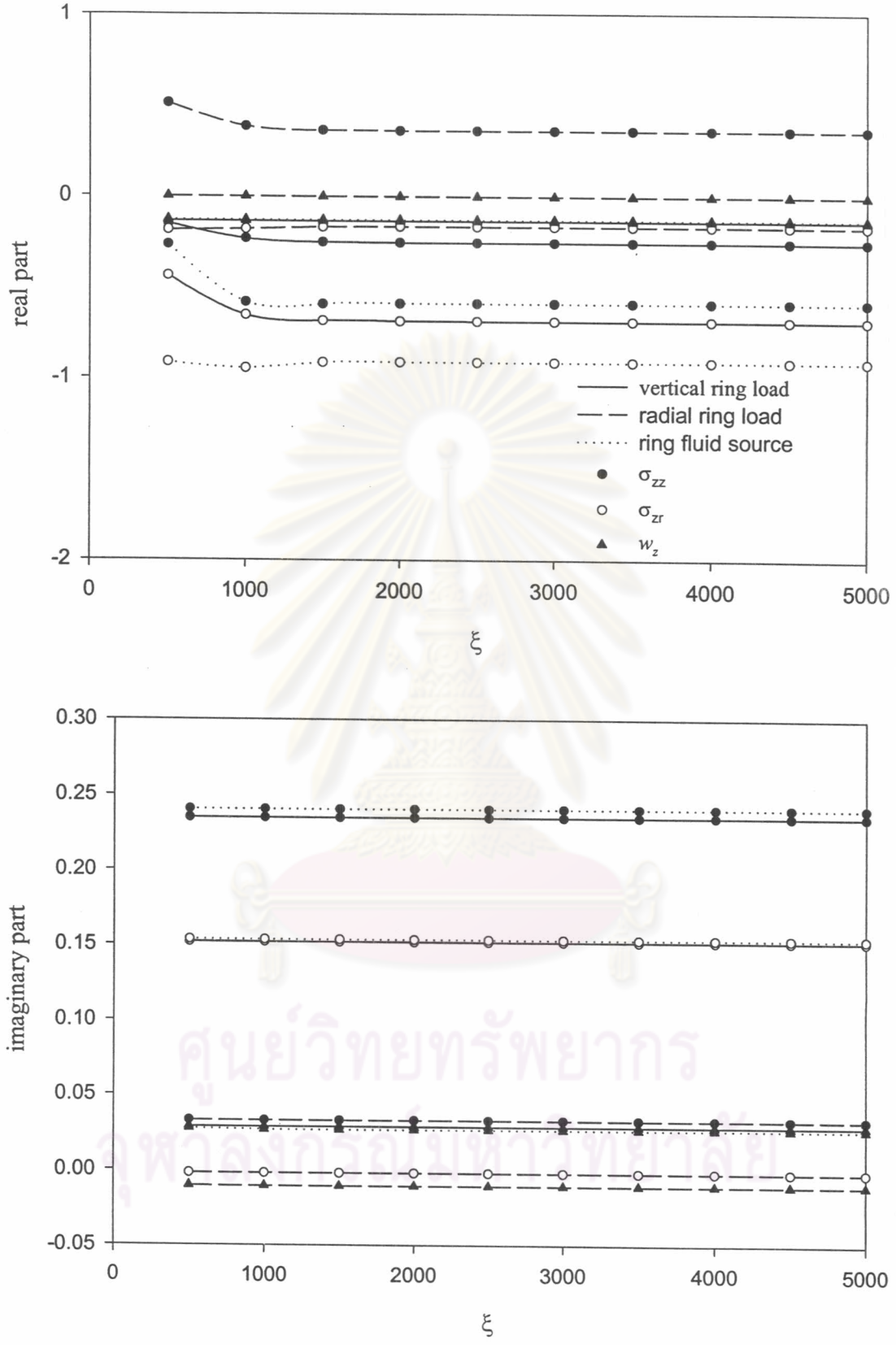

Figure 4.3 Convergence of influence functions subjected to vertical ring load, radial ring load and ring fluid source with respect to ξ_L $\left(|z-z'|=0.005\right)$

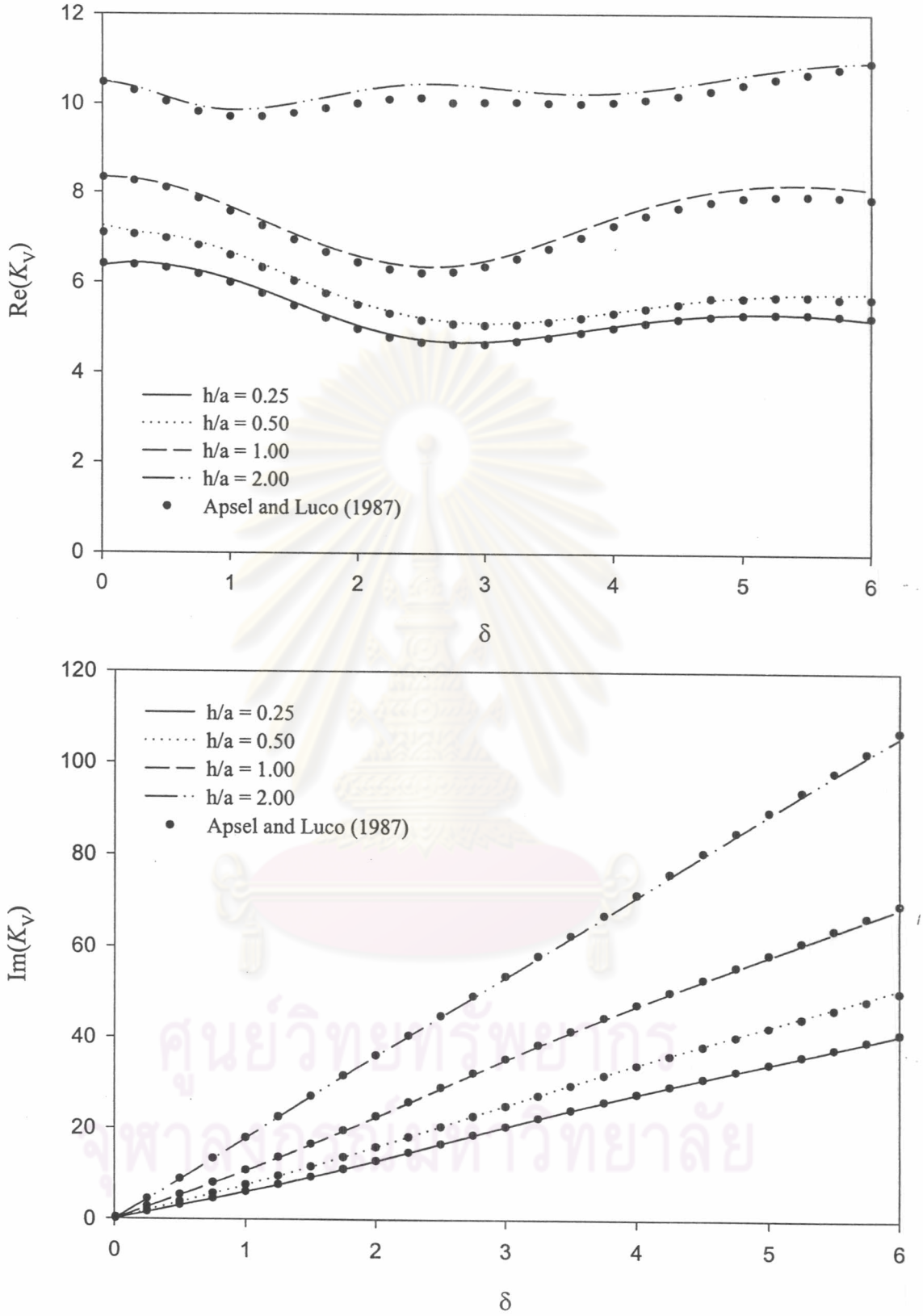

Figure 4.4 Comparison of vertical impedance of a rigid cylinder in elastic half-space with existing solution

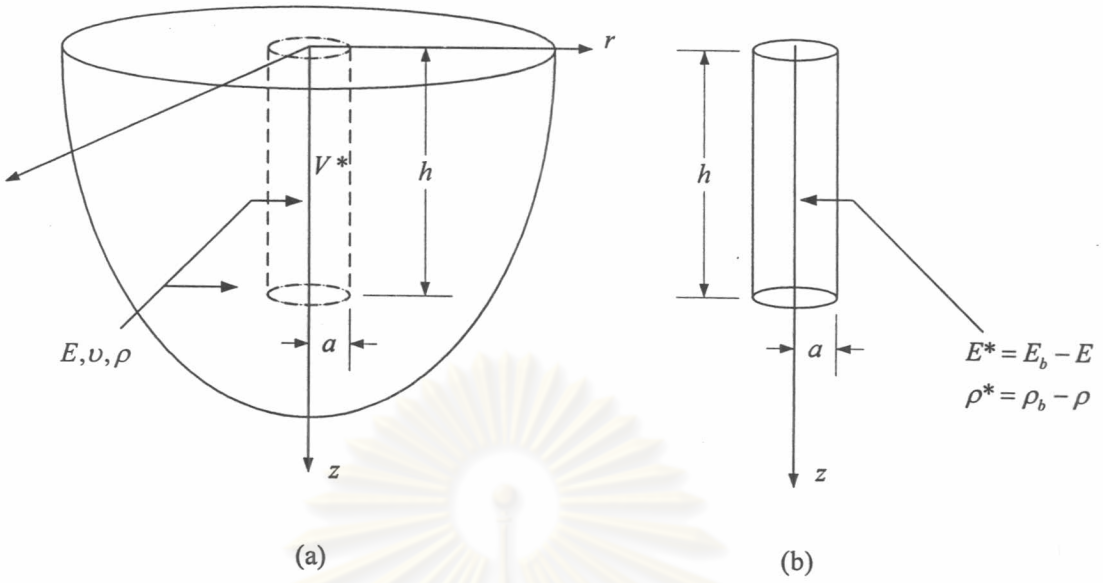

Figure 4.5 (a) Extended half space and (b) fictitious bar

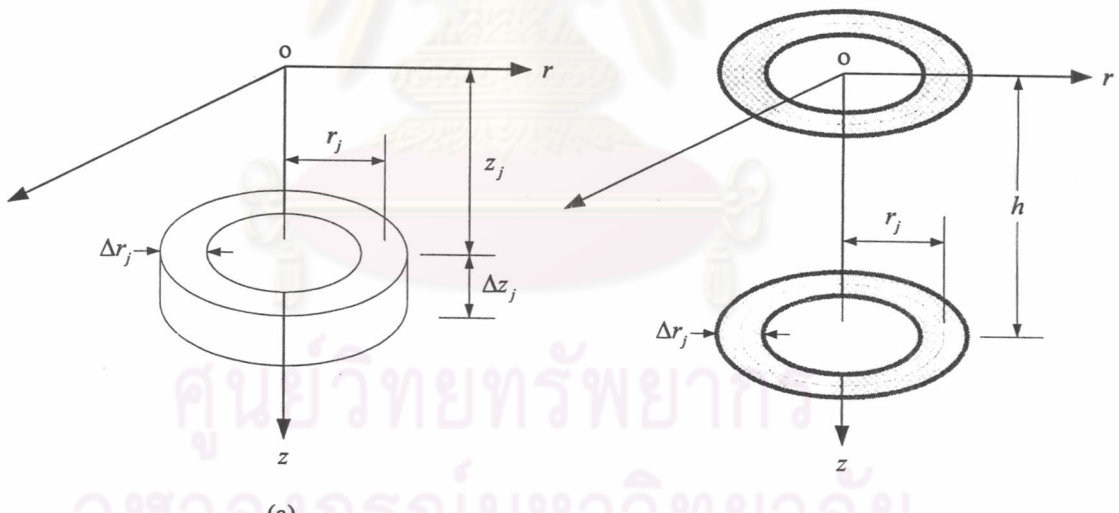

Figure 4.6 Geometry of (a) hollow cylindrical element and (b) base element

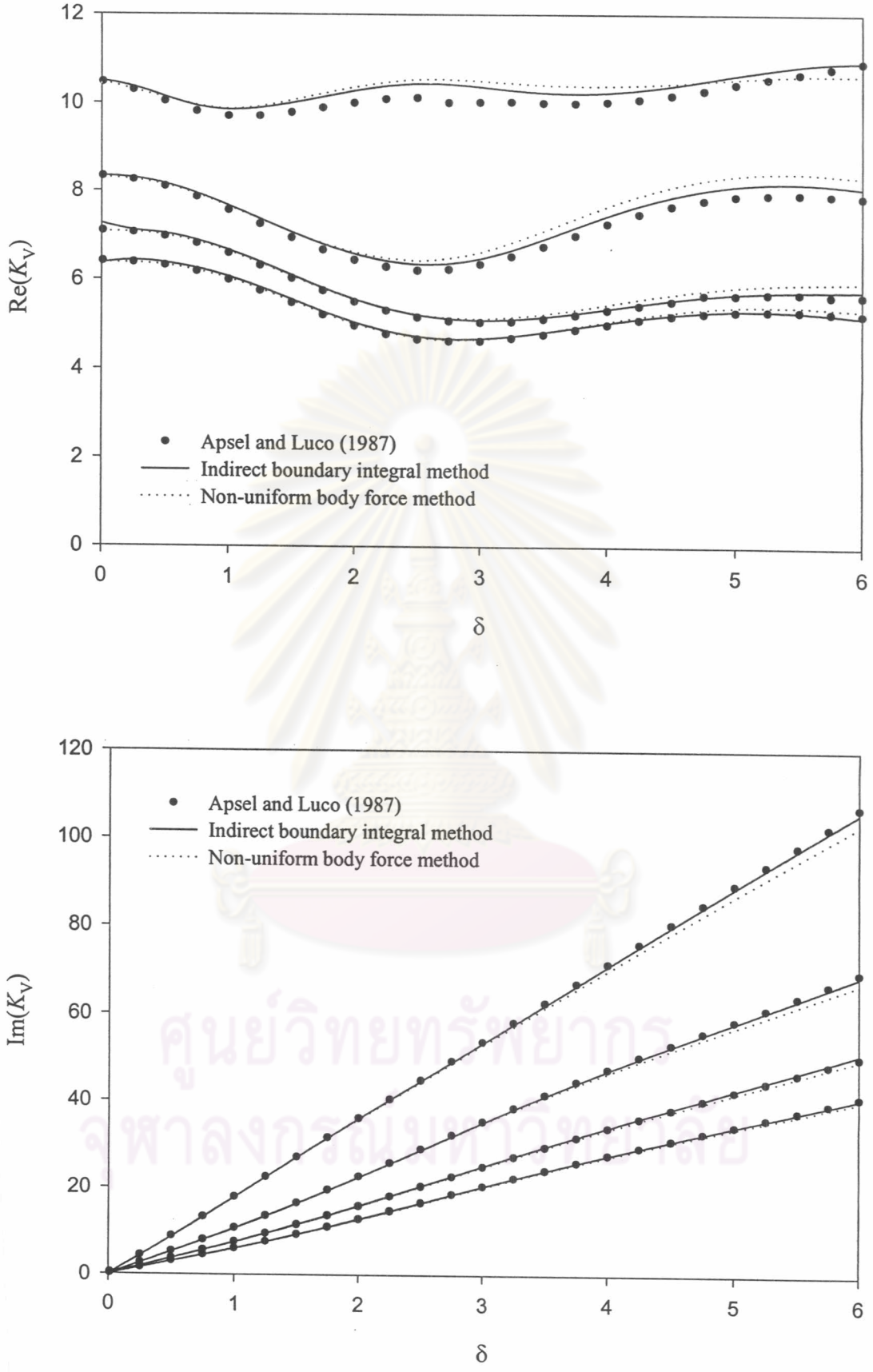

Figure 4.7 Comparison of vertical impedance of a rigid cylinder in elastic half-space for different computation method

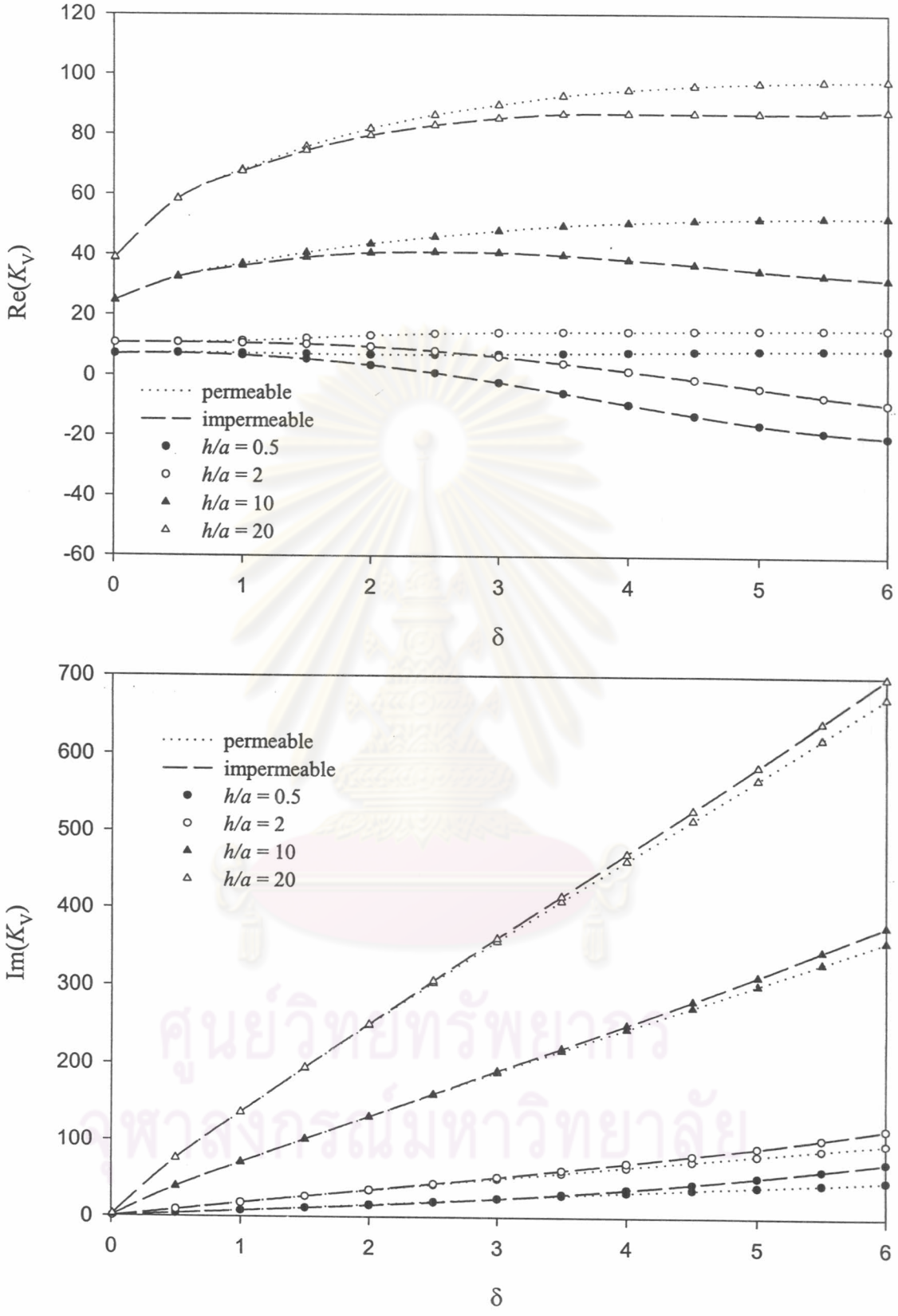

Figure 4.8 Vertical impedance of rigid cylinders for different length/radius ratio ($b^* = 2.3$)

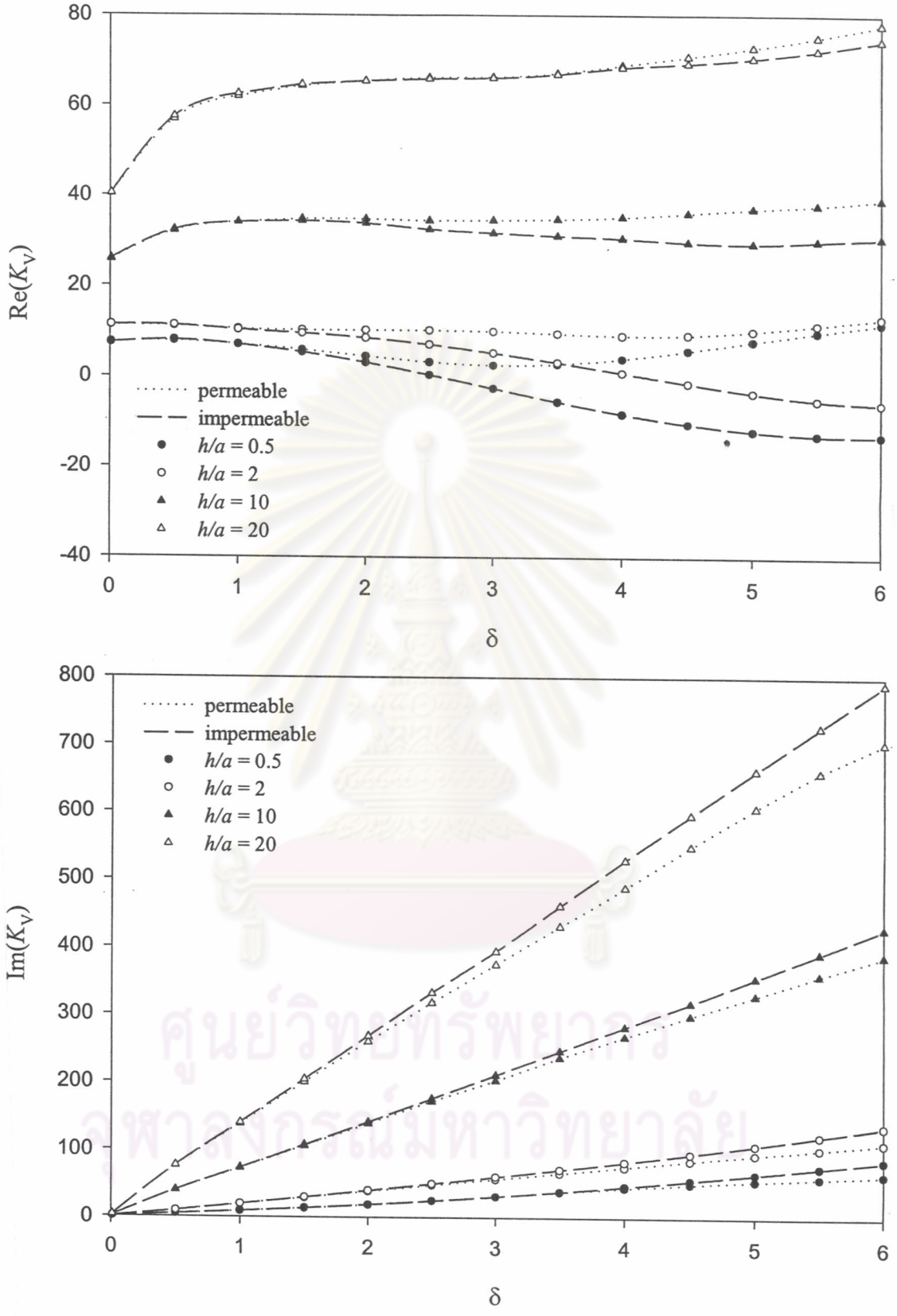

Figure 4.9 Vertical impedance of rigid cylinders for different length/radius ratio ($b^* = 30$)

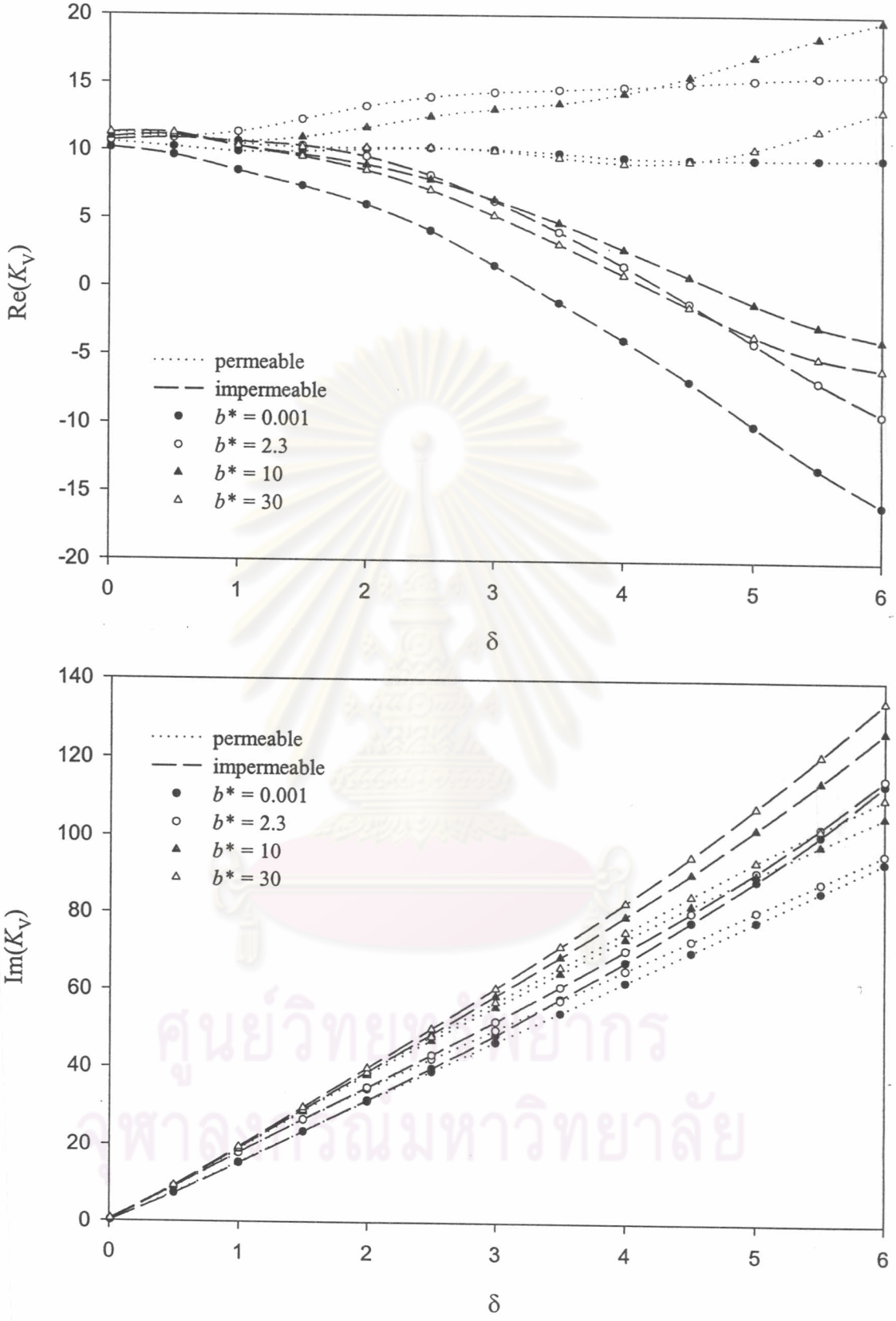

Figure 4.10 Vertical impedance of cylinders for different poroelastic material $(h/a = 2)$

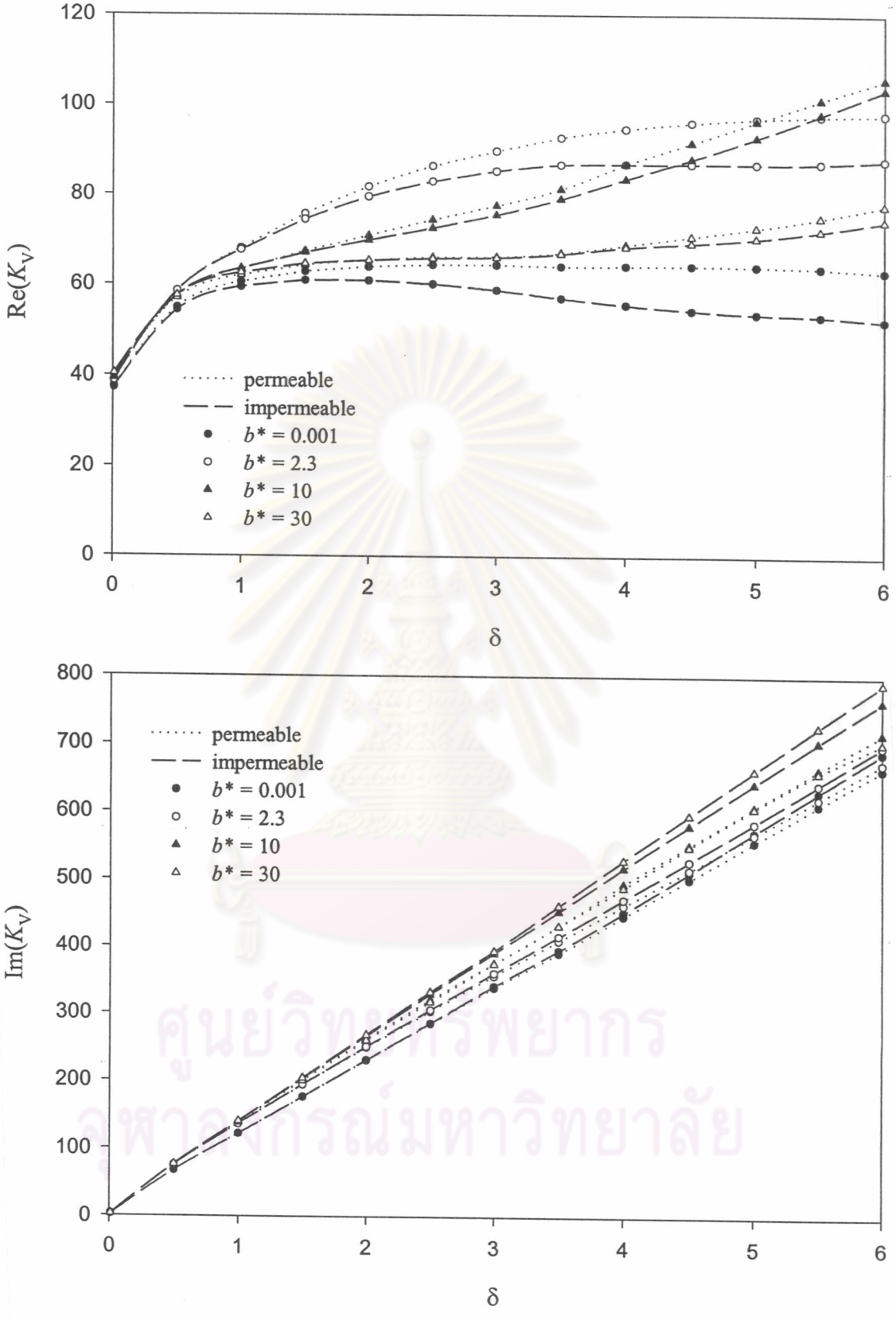

Figure 4.11 Vertical impedance of cylinders for different poroelastic material ($h/a = 20$)

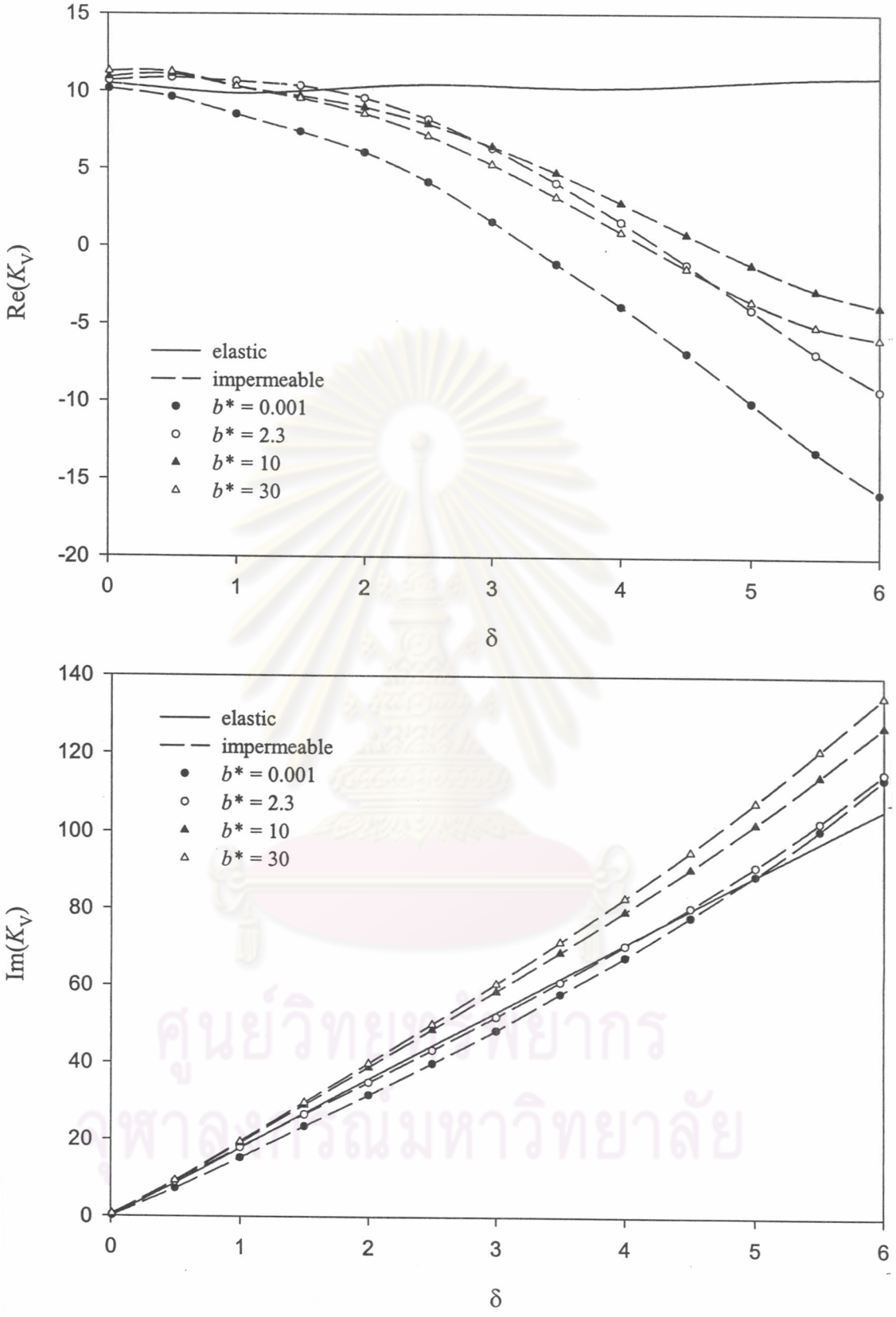

Figure 4.12 Vertical impedance of cylinders for different material $(h/a = 2)$

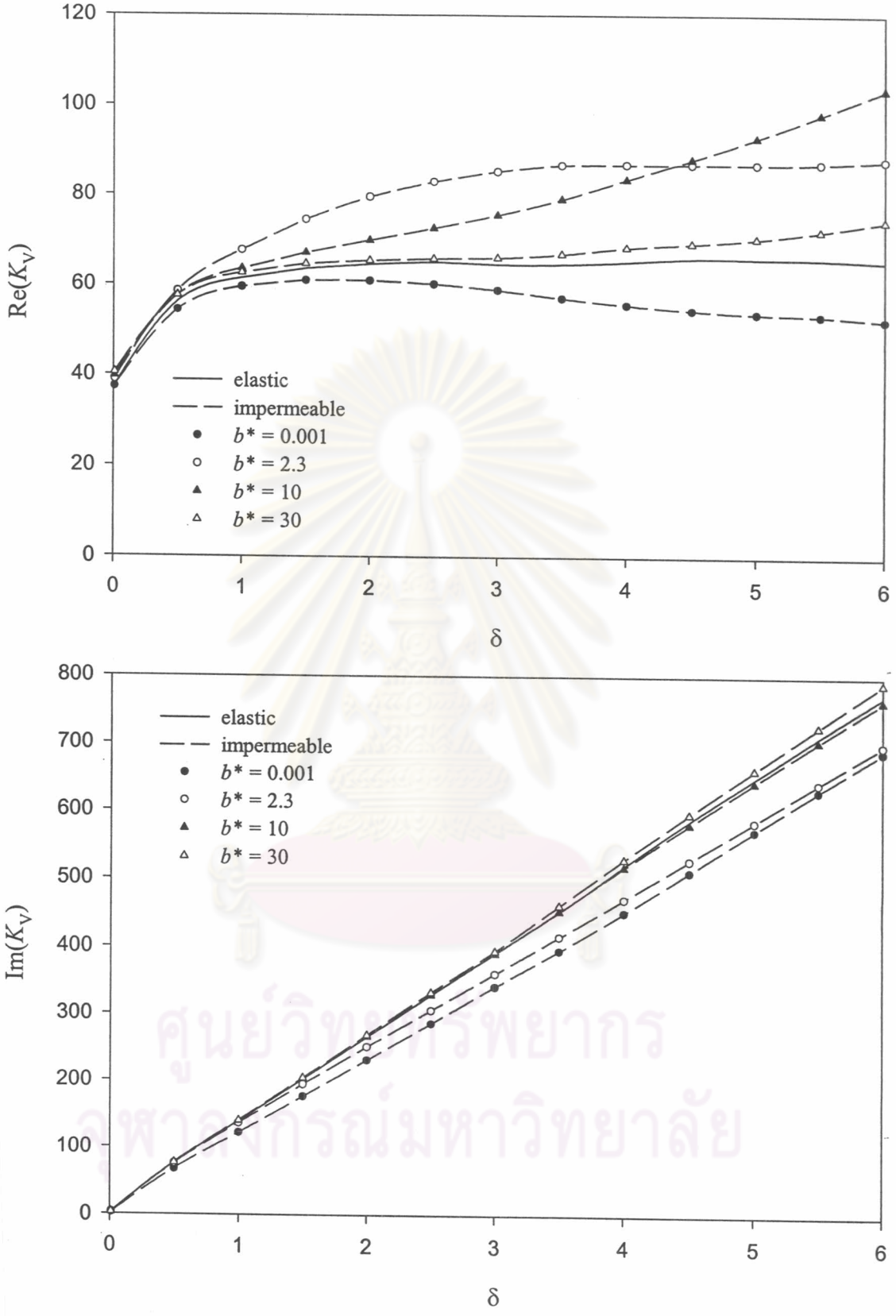

Figure 4.13 Vertical impedance of cylinders for different material $(h/a = 20)$

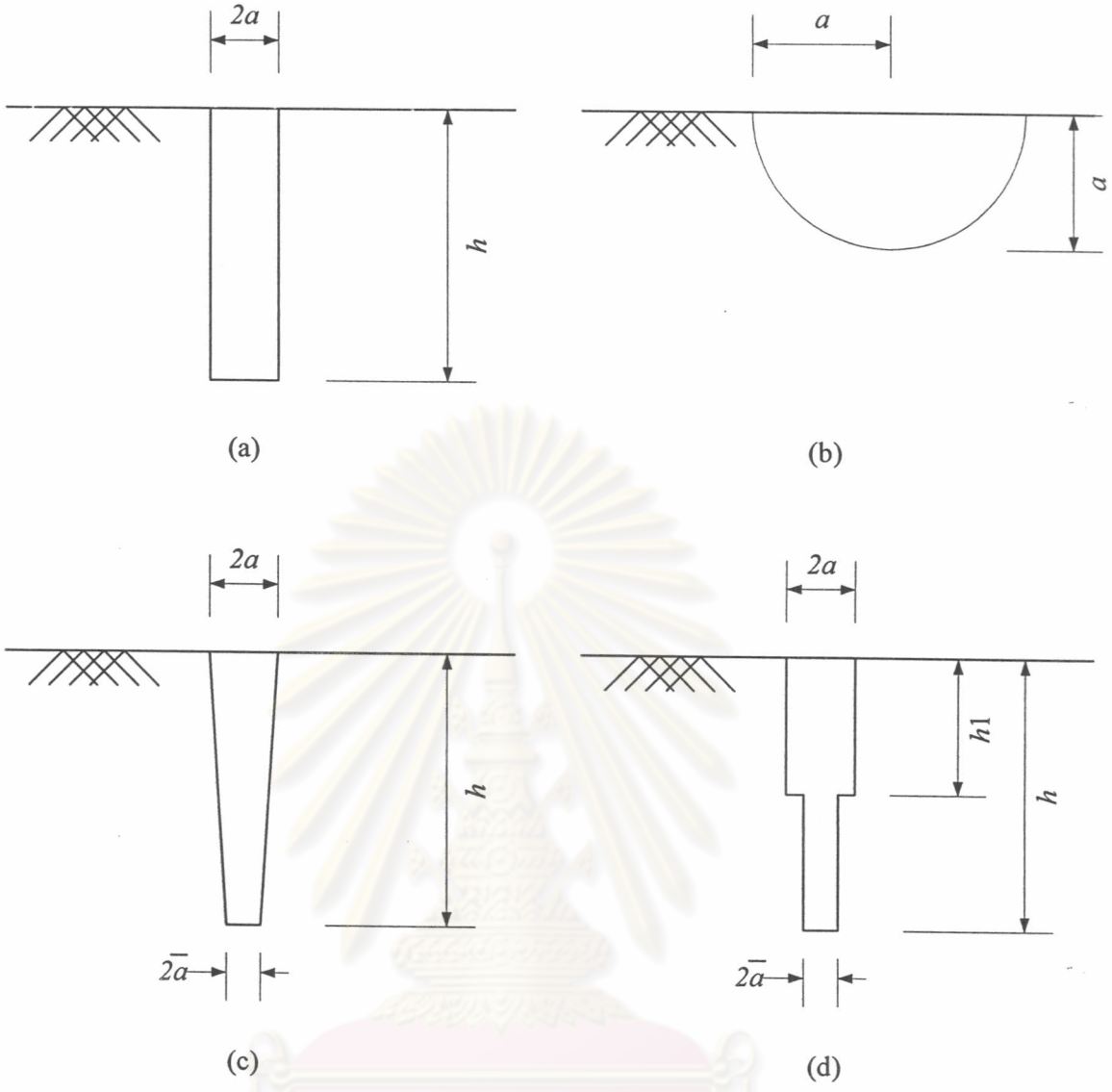

Figure 4.14. The shape of the axisymmetric foundations
(a) cylinder, (b) hemisphere, (c) taper and (d) step

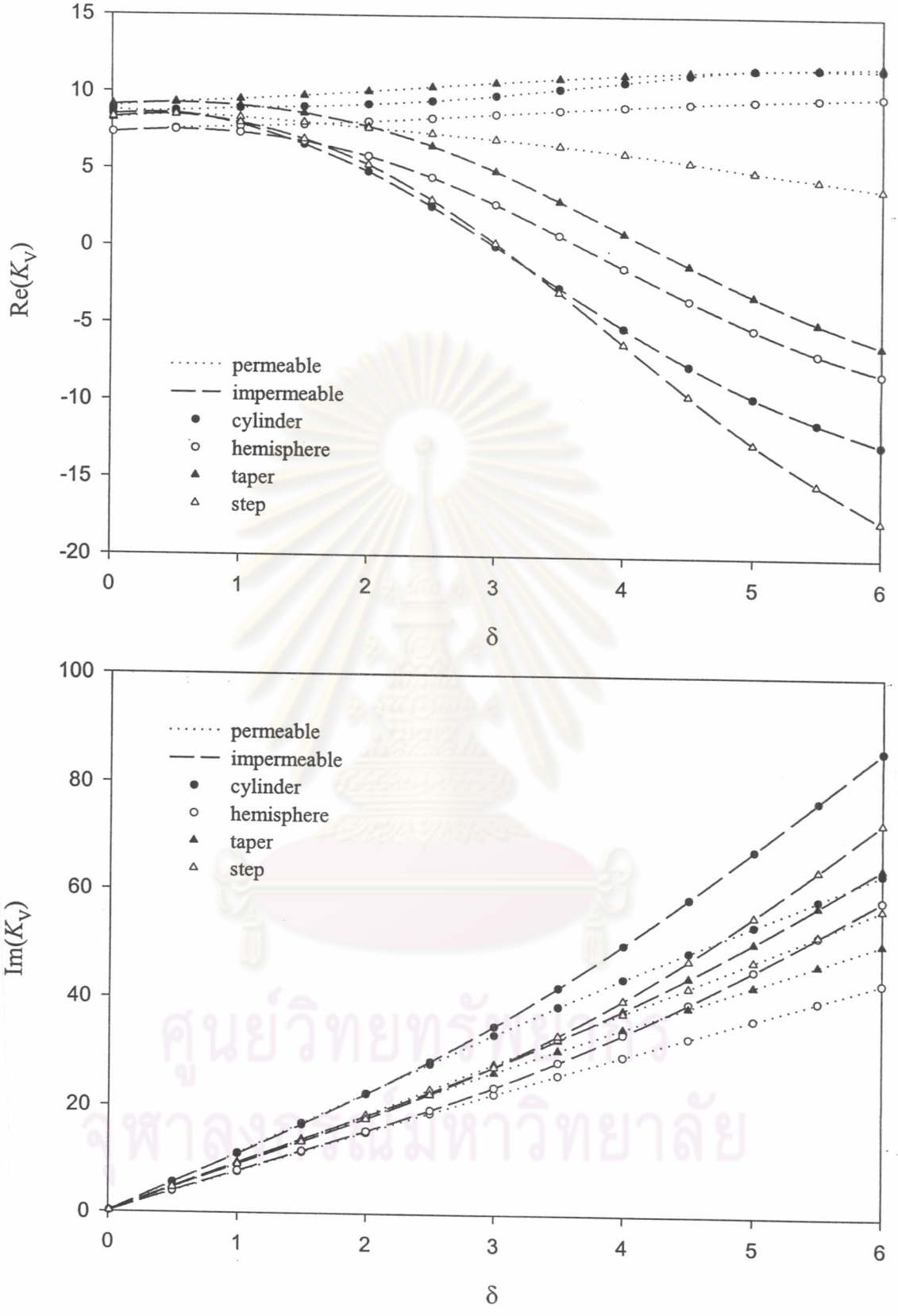

Figure 4.15 Vertical impedance of different shape of the foundation ($b^* = 2.3$)

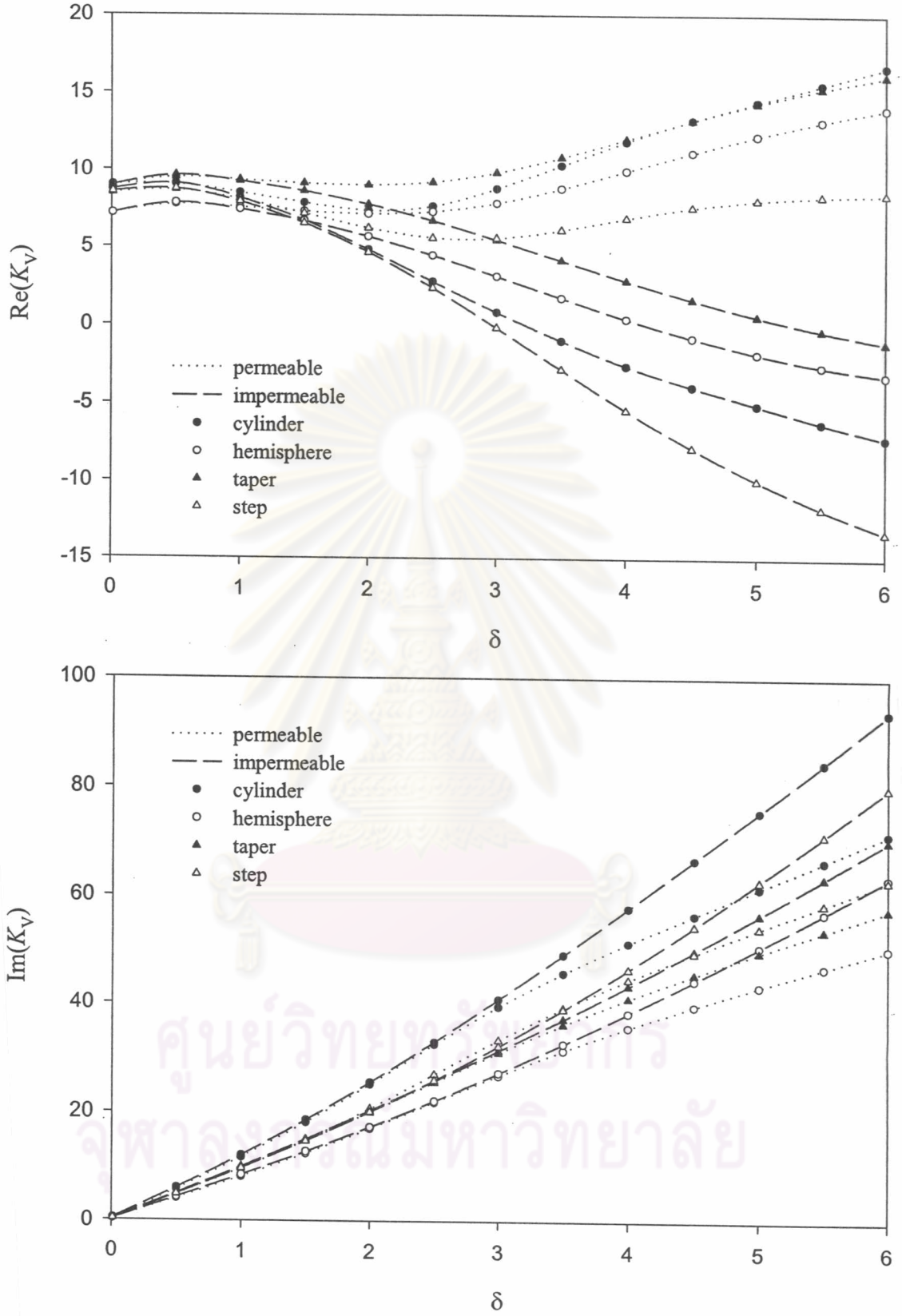

Figure 4.16 Vertical impedance of different shape of the foundation ($b^* = 10$)